



Nonlinear ultrasound in liquid containing multiple coated microbubbles: effect of buckling and rupture of viscoelastic shell on ultrasound propagation

Quoc Nam Nguyen · Tetsuya Kanagawa

Received: 31 August 2022 / Accepted: 2 January 2023 / Published online: 26 April 2023
© The Author(s) 2023

Abstract With promising applications in medical diagnosis and therapy, the behavior of shell-encapsulated ultrasound contrast agents (UCAs) has attracted considerable attention. Currently, second-generation contrast agents stabilized by a phospholipid membrane are widely used and studies have focused on the dynamics of single phospholipid shell-encapsulated microbubbles. To improve the safety and the efficiency of the methods using the propagation or targeted ultrasound, a better understanding of the propagation of ultrasound in liquids containing multiple encapsulated microbubbles is required. By incorporating the Marmottant–Gompertz model into the multiple scale analysis of two-phase model, this study derived a Korteweg–de Vries–Burgers equation as a weakly nonlinear wave equation for one-dimensional ultrasound in bubbly liquids. It was found that the wave propagation characteristics changed with the initial surface tension, highlighting two notable features of the phospholipid shell: buckling and rupture. These results may provide insights into the suitable state of microbubbles, and

better control of ultrasound for medical applications, particularly those that require high precision.

Keywords Encapsulated bubble · Ultrasound contrast agent · Bubble dynamics · Bubbly liquid · Weakly nonlinear theory · Viscoelastic shell

1 Introduction

Since the pioneering research on the collapse of an empty cavity in a liquid by Lord Rayleigh [1] and the extension of bubble dynamics by Plesset [2], researchers have extended the knowledge of single bubble oscillation under driving pressure [3–11]. Another research direction based on bubble dynamics is the study of the propagation of pressure waves in bubbly liquids, which has been performed by various researchers such as van Wijngaarden [12–15] and Caffisch group [16–18]. In recent decades, following the commercialization of ultrasound contrast agents (UCAs), bubble dynamics has received considerable attention, particularly for medical applications such as echocardiography [19–22], drug and gene delivery [23–27], and sonoporation [28–30].

For applications in medical treatment, a comprehensive understanding of the interaction of encapsulated bubbles with ultrasound is required. Several models have been proposed to explain the effect of shells on bubble oscillation, which encapsulate the gas core and provide important functions, such as improvement of

Q. N. Nguyen
Department of Engineering Mechanics and Energy, Degree Programs in Systems and Information Engineering, University of Tsukuba, Tsukuba 305-8573, Japan

T. Kanagawa (✉)
Department of Engineering Mechanics and Energy, Institute of Systems and Information Engineering, University of Tsukuba, Tsukuba 305-8573, Japan
e-mail: kanagawa.tetsuya.fu@u.tsukuba.ac.jp

stability against Laplace-pressure driven dissolution, gas diffusion, and coalescence. For example, de Jong proposed a pioneering model for viscoelastic shells [31–34], Church et al. [35] presented a model for a viscoelastic shell that also incorporates shell thickness, and Hoff et al. constructed a model by considering the limit of shell thickness as zero [35–37]. Furthermore, Chatterjee and Sarkar [38] created a model by assuming that shells behave as Newtonian viscous fluids. Marmottant et al. [39] proposed a model that incorporates the buckling and rupture phenomena, observed in phospholipid monolayer shells (it should be noted that the “rupture” phenomenon defined by Marmottant is not the irreversible collapse in solid mechanics). Recently, a nonlinear viscosity model was suggested by Doinikov et al. [40] and a model incorporating the effect of shell compressibility and anisotropy was developed by Chabouh et al. [41]. Extensive reviews on comparisons and discussions of the models have also been published [42–45]. Under simplifications and assumptions, the existing models show reasonable agreement with experimental results, mostly in the linear regime. However, nonlinear behavior of encapsulated bubbles is complicated, and attempts have been made to better understand these behaviors [46–56]. As Doinikov et al. [57] pointed out, available shell models do not possess required predictive capability for wide range of conditions. This problem may be solved with researches at the molecular scale, using theoretical [58,59] and simulation [60–63] approaches.

Research regarding single encapsulated bubbles in pressure waves is a foundation for studies on ultrasound propagation in a liquid with a large number of encapsulated bubbles. Accordingly, several models have been proposed as an extension of the analysis by van Wijngaarden and Caffisch, and multiple imaging techniques have been developed [64–67]. Ma et al. [68] derived a nonlinear evolution equation for ultrasound propagation in liquids containing multiple encapsulated bubbles, and Xia [69] theoretically studied the attenuation coefficient of ultrasound propagation. These studies, however, were limited to linear case and cannot holistically reflect nonlinear effects such as rapid attenuation change above the Blake threshold or the dependence on pressure of attenuation and sound speed. To address such limitations, in his pioneering paper, Louisnard [70,71] constructed a mechanical energy balance equation from fully nonlinear Caffisch equations. Here, energy loss was computed numerically by simu-

lating bubble radial dynamics Rayleigh–Plesset equation. Consequently, a nonlinear Helmholtz equation for wave propagation in liquids with uncoated bubbles was derived. Accordingly, pressure dependent attenuation was derived from the imaginary part of wave number. This equation is relatively easier to solve than the fully nonlinear Caffisch equations and can predict more realistic attenuation and acoustic pressure values compared to the fully linearized models. Similarly, Jamshidi et al. [72] considered compressibility of the liquid using Keller–Miksis equation, and the additional attenuation effect of acoustic radiation was obtained in addition to small modifications to thermal and viscosity attenuation terms. Later, the Jamshidi model was shown to have non-physical values and a critical modification to the calculation of the damping terms was provided by Sojahrood et al. [73]. These values had better agreement with the linear model and resolved the non-physical values. Additionally, they extended previous studies and were the first to introduce a full nonlinear model capable of simultaneously calculating the pressure dependence of sound speed, which affected local acoustic pressure amplitude, and attenuation [74]. This model was verified numerically [75] and in the first controlled observation of the pressure dependence of sound speed and attenuation for coated bubbles [76]. To describe wave propagation in a liquid containing a high number of viscoelastic shell-encapsulated microbubbles, we have adopted another approach using two-phase model. Consequently, the Korteweg–de Vries–Burgers (KdVB) equations were obtained [77–79]. Although our studies are limited to small pressure amplitude, the proposed models can account for the nonlinear propagation of waves, a characteristic neglected in models based on the Helmholtz model.

The buckling and rupture of the shell were first modeled by Marmottant et al. [39] for large-amplitude oscillations of coated bubbles. Researchers using this model have reported that it can predict important behaviors exhibited by phospholipid monolayer shells. De Jong et al. [80] observed a highly nonlinear response of phospholipid-coated UCA termed “compression-only” behavior, wherein microbubbles compressed but barely expanded beyond its initial radius. Later, Emmer et al. [81] linked the “compression-only” behavior to the enhanced second harmonic behavior, and Sijl et al. [48] theoretically showed that the subharmonic behavior and its threshold pressure can be explained through

the value and rate of change of elasticity with radius, which are important features of the Marmottant model. The Marmottant model has been demonstrated to have predicted the intensification of the generation of 1/2 order subharmonics via simulation and experiment on bubbles in the buckling region [49]. Several researchers have reported the change in resonance curves and onset of vibrations [82,83]. These two prominent nonlinear effects were explained later using the Marmottant model by Overvelde et al. [47]. Recently, the generation of higher order subharmonics (e.g., 1/3, 1/4) has been demonstrated by analyzing bifurcation structure and verified experimentally by Sojahrood et al. [84]. Since many approved UCAs for human use such as Definity (2001), SonoVue (2001), and Sonazoid (2007) are coated by phospholipid shells, the incorporation of the two physical properties (buckling and rupture) is necessary to model the interaction between ultrasound and phospholipid shell encapsulated microbubbles.

The aim of the present paper is to extend previous studies on ultrasound propagation in liquids containing multiple microbubbles encapsulated with viscoelastic shell [77] or with compressible viscoelastic shell [78,79], by incorporating buckling and rupture phenomena. To the best of our knowledge, this is the first theoretical study that considers effect of buckling and rupture of phospholipid shell on ultrasound propagation in a liquid containing multiple encapsulated bubbles that includes nonlinearity parameters through two-phase model. Instead of the original model proposed by Marmottant et al. [39], we consider the Marmottant–Gompertz model [85] to describe the behavior of the surface tension of the phospholipid shell, as the latter offers important features relevant to our study (as described in Sect. 2.2). Following the method described in our previous papers [86,87], we derived a KdVB equation as a physico-mathematical model for ultrasound propagation.

The remainder of this paper is organized as follows. Section 2 introduces basic equations for bubbly liquids based on a two-fluid model [88] and lipid-encapsulated bubble dynamics including shell buckling and rupture. Section 3 presents derivation of linear propagation for the first-order problem and a KdVB equation for the second-order problem. Section 4 presents a parametric analysis conducted to explore the effect of the initial void fraction and initial surface tension on the characteristics of the propagation (i.e., advective

tion, nonlinearity, attenuation and dispersion). Furthermore, the results obtained after the analysis proposed by Katiyar and Sarkar [50], with the upper and lower limits of the surface tension removed, are presented. The limitations of derived model are then discussed. Finally, Sect. 5 presents the conclusions of this paper.

2 Problem formulation

2.1 Problem statement

We consider a weakly nonlinear (i.e., finite but small amplitude) propagation of plane and progressive pressure waves radiating from a source in a bubbly liquid.

In this study, the following assumptions were made for simplicity:

- (i) The liquid is slightly compressible.
- (ii) The initial flow velocities of gas and liquid phases are zero.
- (iii) The number of bubbles is constant, i.e., the bubbles do not coalesce, break up, appear, and disappear.
- (iv) Only one bubble size is considered, and the bubble distribution is spatially uniform.
- (v) Bubble–bubble interaction is neglected.
- (vi) The mass transport through the bubble–liquid interface is neglected, i.e., the number of molecules inside the gas core of each bubble is constant.
- (vii) The bubble oscillations are spherically symmetric and are the same in an averaged volume.
- (viii) The translation of bubbles and drag force on the bubbles are neglected.
- (ix) The thermal conductivity and phase change are neglected.
- (x) Shell viscosity is considered, and liquid viscosity is only considered at the bubble–liquid interface.
- (xi) The temperature of the liquid is constant.
- (xii) The buckling and rupture are accounted for.

Except for assumption (xii), which is the main topic of this study, the other assumptions are identical to those in our previous papers [86–88]. The buckling and rupture of the shell were modeled using the Marmottant–Gompertz model, first suggested by Gümmer et al. [85].

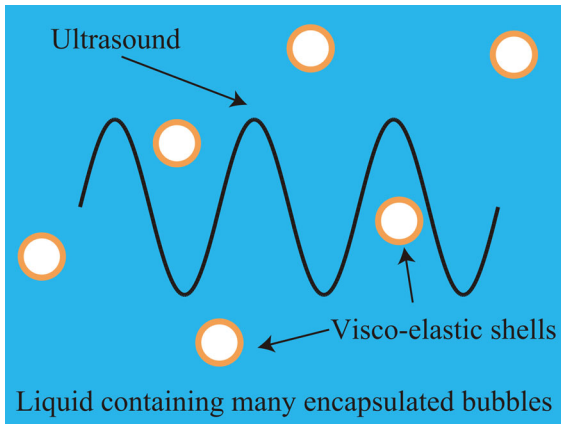


Fig. 1 Schematic of model: Ultrasound propagation in liquid containing multiple microbubbles coated by a viscoelastic shell with buckling and rupture

2.2 Governing equations

In this study, we use a two-fluid model [88, 89] structured by a set of basic equations. This set includes the following equations:

- (i) Mass conservation law in the gas phase

$$\frac{\partial}{\partial t^*}(\alpha \rho_G^*) + \frac{\partial}{\partial x^*}(\alpha \rho_G^* u_G^*) = 0. \tag{1}$$

- (ii) Mass conservation law in the liquid phase

$$\frac{\partial}{\partial t^*}[(1 - \alpha) \rho_L^*] + \frac{\partial}{\partial x^*}[(1 - \alpha) \rho_L^* u_L^*] = 0. \tag{2}$$

- (iii) Momentum conservation law in the gas phase

$$\frac{\partial}{\partial t^*}(\alpha \rho_G^* u_G^*) + \frac{\partial}{\partial x^*}(\alpha \rho_G^* u_G^{*2}) + \alpha \frac{\partial p_G^*}{\partial x^*} = F^*. \tag{3}$$

- (iv) Momentum conservation law in the liquid phase

$$\begin{aligned} \frac{\partial}{\partial t^*}[(1 - \alpha) \rho_L^*] + \frac{\partial}{\partial x^*}[(1 - \alpha) \rho_L^* u_L^{*2}] \\ + (1 - \alpha) \frac{\partial p_L^*}{\partial x^*} + P^* \frac{\partial \alpha}{\partial x^*} = -F^*, \end{aligned} \tag{4}$$

where α is the void fraction (the gas fraction) ($0 < \alpha < 1$), ρ^* is the density, u^* is the velocity, p^* is the pressure, and the subscripts G and L indicate the volume-averaged variables in the gas and liquid phases, respectively. The right-hand sides of Eqs. (3) and (4) show the interfacial momentum transport, denoted as F^* , following the model of virtual mass force in a compressible liquid [89–91]

$$\begin{aligned} F^* = & -\beta_1 \alpha \rho_L^* \left(\frac{D_G u_G^*}{D t^*} - \frac{D_L u_L^*}{D t^*} \right) \\ & -\beta_2 \rho_L^* (u_G^* - u_L^*) \frac{D_G \alpha}{D t^*} - \beta_3 \alpha (u_G^* - u_L^*) \frac{D_G \rho_L^*}{D t^*}, \end{aligned} \tag{5}$$

For spherical bubble case, the coefficients β_1 , β_2 and β_3 can be set to 1/2. We refrained from explicitly using these values to present the contribution of each term to the result. The total derivatives are defined as follows:

$$\begin{aligned} \frac{D_G}{D t^*} & \equiv \frac{\partial}{\partial t^*} + u_G^* \frac{\partial}{\partial x^*}, \\ \frac{D_L}{D t^*} & \equiv \frac{\partial}{\partial t^*} + u_L^* \frac{\partial}{\partial x^*}, \end{aligned} \tag{6}$$

- (v) Modified Rayleigh–Plesset equation for spherical oscillations of bubbles in a slightly compressible liquid [39]

$$\begin{aligned} \rho_{L0}^* R^* \frac{D_G^2 R^*}{D t^{*2}} + \rho_{L0}^* \frac{3}{2} \left(\frac{D_G R^*}{D t^*} \right)^2 \\ = P^* + \frac{R^*}{c_{L0}^*} \frac{D_G}{D t^*} p_G^*, \end{aligned} \tag{7}$$

where R^* is the bubble radius, ρ_{L0}^* is the liquid density in unperturbed state, c_{L0}^* is the initial sound velocity in the liquid phase and P^* is the difference between volume-averaged liquid pressure and liquid pressure at bubble surface. Equations (1)–(5) and (7) are closed using the following equations:

- (vi) Tait equation of state for liquid

$$p_L^* = p_{L0}^* + \frac{\rho_{L0}^* c_{L0}^{*2}}{n} \left[\left(\frac{\rho_L^*}{\rho_{L0}^*} \right)^n - 1 \right], \tag{8}$$

- (vii) Polytopic equation of state for gas

$$\frac{p_G^*}{p_{G0}^*} = \left(\frac{\rho_G^*}{\rho_{G0}^*} \right)^\gamma, \tag{9}$$

- (viii) Conservation law of mass inside a bubble

$$\frac{\rho_G^*}{\rho_{G0}^*} = \left(\frac{R_0^*}{R^*} \right)^3, \tag{10}$$

where p_{L0}^* and R_0^* are the liquid pressure and bubble radius, respectively, in the initial undisturbed state; p_{G0}^* and ρ_{G0}^* are the gas pressure and density inside the bubble in the initial state, respectively; γ is the polytropic exponent; and n is the material constant (e.g., $n = 7.15$ for water).

- (ix) The equation for balance of the normal stress across bubble–liquid interface based on the equation given by Marmottant et al. [39]

$$p_G^* - (p_L^* + P^*) = \frac{2\sigma^*(R^*)}{R^*} + \frac{4\mu^*}{R^*} \frac{D_G R^*}{D t^*}$$

$$+ \frac{4\kappa_s^* D_G R^*}{R^{*2} D t^*}, \tag{11}$$

Here, μ^* is the liquid viscosity, and κ_s^* is the shell dilatational viscosity derived for shells with small but finite and constant thickness.

To incorporate the buckling and rupture phenomena in our study, instead of using the original model of surface tension proposed by Marmottant et al. [39], in which there are two discontinuities at $R^* = R_{\text{buck}}^*$ and $R^* = R_{\text{rupt}}^*$, we use the continuous Marmottant–Gompertz model constructed by Gümmer et al. [85], the detailed form of this model is given in “Appendix A” (Fig. 2).

The Marmottant model can simulate certain nonlinear characteristics such as “compression-only” and subharmonic behaviors of phospholipid-coated microbubbles [43–45, 47–49]. The Marmottant surface tension model has two important features: the first are an upper limit (ruptured state) and a zero lower limit (buckled state). The effects of these limits on the excitation threshold for subharmonic generation were studied by Katiyar and Sarkar [50]. The second is the rapid change of the elastic coefficient χ^* between the elastic-buckled state and elastic-ruptured state with two singularities of $d\chi^*/dR^*$ at $R^* = R_{\text{buck}}^*$ and $R^* = R_{\text{rupt}}^*$. These two singularities make the Marmottant model sensitive to the time step used in numerical methods [48, 85]. To resolve this sensitivity, Silj et al. [48] proposed two additional quadratic crossover functions to smoothen the curve and control the two transition points. The Marmottant–Gompertz model proposed by Gümmer et al. [85] is based on the Gompertz function. This model can smoothen the curve and eliminate the singularities using the same set of initial parameters (i.e., R_0^* , χ^* and σ_0^*), while retaining the two significant features of the Marmottant model. The elimination of these two singularities allows for the calculation of the continuous first and second derivatives of the function. Accordingly, the linearization for theoretical analysis can be obtained. Furthermore, without the singularities, the sensitivity to the time step in numerical calculations is dismissed. As an inherent characteristic of the Gompertz function, there is a more rapid change of surface tension near buckled radius than near ruptured radius, providing good qualitative approximation to the behavior of the lipid monolayer observed in experiments. Additionally, the Marmottant–Gompertz equation is shown to have no significant difference to the original Marmottant model for acoustic emissions and overall dynam-

ics of the bubble while demonstrating smoother bubble radius transition in and out of the elastic regime. The result also has good agreement to *in vitro* experiments under similar conditions. Readers are referred to Gümmer et al. [85] for further discussion of the Marmottant–Gompertz model.

2.3 Multiple-scale analysis

For weakly nonlinear problems, the nonlinear effect becomes apparent at a large distance from the sound source relative to the wavelength. In these problems, different time and length scales are considered. First, the independent variables are nondimensionalized as

$$t = \frac{t^*}{T^*}, \quad x = \frac{x^*}{L^*}, \tag{12}$$

where T^* and L^* are the typical period and wavelength of the propagating wave, respectively. Then, the near-field (i.e., the temporal and spatial scales of $\mathcal{O}(1)$) is defined as

$$t_0 = t, \quad x_0 = x, \tag{13}$$

and the far-field (i.e., the temporal and spatial scales of $\mathcal{O}(1/\epsilon)$) is described as

$$t_1 = \epsilon t, \quad x_1 = \epsilon x, \tag{14}$$

where ϵ is the nondimensional wave amplitude under the assumption ($0 < \epsilon \ll 1$). Using Eqs. (13) and (14) with the derivative-expansion method [92], the differential operators are expanded as follows:

$$\begin{aligned} \frac{\partial}{\partial t} &= \frac{\partial}{\partial t_0} + \epsilon \frac{\partial}{\partial t_1}, \\ \frac{\partial}{\partial x} &= \frac{\partial}{\partial x_0} + \epsilon \frac{\partial}{\partial x_1}. \end{aligned} \tag{15}$$

Further, the dependent variables are nondimensionalized and expanded in the power series of ϵ :

$$\frac{\alpha}{\alpha_0} = 1 + \epsilon \alpha_1 + \epsilon^2 \alpha_2 + \dots, \tag{16}$$

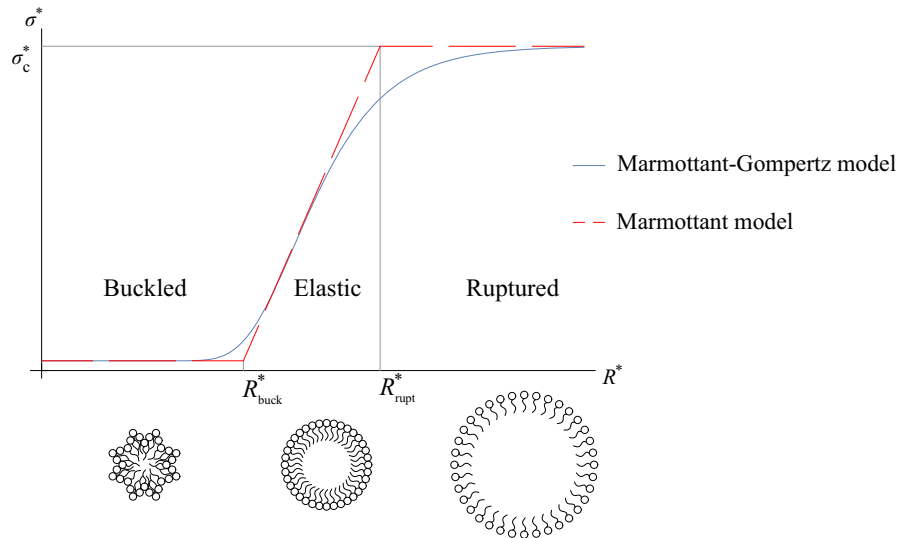
$$\frac{R^*}{R_0^*} = 1 + \epsilon R_1 + \epsilon^2 R_2 + \dots, \tag{17}$$

$$\frac{\rho_L^*}{\rho_{L0}^*} = 1 + \epsilon^2 \rho_{L1} + \epsilon^3 \rho_{L2} + \dots, \tag{18}$$

$$\frac{p_L^*}{\rho_{L0}^* U^{*2}} = p_{L0} + \epsilon p_{L1} + \epsilon^2 p_{L2} + \dots, \tag{19}$$

$$\frac{u_G^*}{U^*} = \epsilon u_{G1} + \epsilon^2 u_{G2} + \dots, \tag{20}$$

Fig. 2 Comparison of Marmottant–Gompertz surface tension model [85] (blue solid curve) and Marmottant surface tension model [39] (red dashed curve). R^* is bubble radius, σ^* surface tension, R_{buck}^* buckle radius, R_{rupt}^* rupture radius, σ_c^* surface tension of the clean gas–liquid interface



$$\frac{u_L^*}{U^*} = \epsilon u_{L1} + \epsilon^2 u_{L2} + \dots, \tag{21}$$

where α_0 is the initial void fraction and U^* is the typical wave propagation speed, which is related to the wavelength L^* and period T^* through $U^* \equiv L^*/T^*$.

The nondimensional pressures for the gas and liquid phases in the unperturbed states p_{G0} and p_{L0} are defined as:

$$p_{G0} \equiv \frac{p_{G0}^*}{\rho_{L0}^* U^{*2}} \equiv \mathcal{O}(1), \quad p_{L0} \equiv \frac{p_{L0}^*}{\rho_{L0}^* U^{*2}} \equiv \mathcal{O}(1). \tag{22}$$

The liquid viscosity μ^* , shell viscosity κ_s^* and initial surface tension σ_0^* are nondimensionalized as

$$\frac{\mu^*}{\rho_{L0}^* U^* L^*} \equiv \mathcal{O}(\epsilon) \equiv \mu\epsilon, \tag{23}$$

$$\frac{\kappa_s^*}{\rho_{L0}^* U^{*2} R_0^* T^*} \equiv \mathcal{O}(\epsilon) \equiv \kappa_s \epsilon, \tag{24}$$

$$\frac{\sigma_0^*}{\rho_{L0}^* U^{*2} R_0^*} \equiv \mathcal{O}(1) \equiv \sigma_0. \tag{25}$$

For simplicity, we define the following two parameters:

$$\frac{\sigma_c^*}{2\chi^*} \equiv \mathcal{O}(1) \equiv \chi_c, \tag{26}$$

$$\frac{\sigma_0^*}{\chi^*} \equiv \mathcal{O}(1) \equiv \chi_0. \tag{27}$$

Using Marmottant–Gompertz model, the surface tension σ^* can be expanded as follows:

$$\sigma^* = \sigma_0^* \left[1 + \epsilon N_1 R_1 + \epsilon^2 (N_{22} R_2 + N_{21} R_1^2) \right], \tag{28}$$

where the explicit forms of N_1 , N_{22} and N_{21} are

$$N_1 = N_{22} \equiv -\ln\left(\frac{\chi_0}{2\chi_c}\right) \frac{e}{\chi_c} \sqrt{(1 + \chi_0)(1 + \chi_c)} \\ = \frac{1}{\sigma_0^*} \left. \frac{\partial \sigma^*}{\partial (R^*/R_0^*)} \right|_{R^*/R_0^*=1}, \tag{29}$$

$$N_{21} \equiv \frac{1}{2} \frac{e^2}{\chi_c^2} (1 + \chi_0)(1 + \chi_c) \left(\ln \frac{\chi_0}{2\chi_c} + \ln^2 \frac{\chi_0}{2\chi_c} \right) \\ = \frac{1}{\sigma_0^*} \left. \frac{\partial^2 \sigma^*}{\partial (R^*/R_0^*)^2} \right|_{R^*/R_0^*=1}. \tag{30}$$

Substitute Eq. (28) into the modified Rayleigh–Plesset equation (Eq. (7)), and follow the analysis of Van der Meer et al. [82], the eigenfrequency of the bubble is obtained through linearization:

$$\omega_B^{*2} = \frac{1}{\rho_{L0}^* R_0^{*2}} \left[\frac{2\sigma_0^* (N_1 - 1)}{R_0^*} + 3p_{G0}^* \gamma \right]. \tag{31}$$

We focus on the long-range propagation of nonlinear waves in low-frequency and long-wavelength bands. In this case, the appropriate scaling relations [86] are

$$\frac{U^*}{c_{L0}^*} \equiv \mathcal{O}(\sqrt{\epsilon}) \equiv V\sqrt{\epsilon}, \tag{32}$$

$$\frac{R_0^*}{L^*} \equiv \mathcal{O}(\sqrt{\epsilon}) \equiv \Delta\sqrt{\epsilon}, \tag{33}$$

$$\frac{\omega^*}{\omega_B^*} \equiv \frac{1}{T^* \omega_B^*} \equiv \mathcal{O}(\sqrt{\epsilon}) \equiv \Omega \sqrt{\epsilon}, \tag{34}$$

where V , Δ and Ω are of order unity, and ω^* is the typical angular frequency.

3 Derivation of KdVB equation

3.1 Leading order of approximation

Substituting Eqs. (5), (6), (8)–(25), and (28)–(34) into Eqs. (1)–(4) and (7) and collecting the ϵ^1 terms, the following set of linearized equations for the first-order problem is obtained:

(i) Mass conservation equation in the gas phase

$$\frac{\partial \alpha_1}{\partial t_0} - 3 \frac{\partial R_1}{\partial t_0} + \frac{\partial u_{G1}}{\partial x_0} = 0, \tag{35}$$

(ii) Mass conservation law in the liquid phase

$$\alpha_0 \frac{\partial \alpha_1}{\partial t_0} - (1 - \alpha_0) \frac{\partial u_{L1}}{\partial x_0} = 0, \tag{36}$$

(iii) Momentum conservation law in the gas phase

$$\beta_1 \frac{\partial u_{G1}}{\partial t_0} - \beta_1 \frac{\partial u_{L1}}{\partial t_0} - 3\gamma p_{G0} \frac{\partial R_1}{\partial x_0} = 0, \tag{37}$$

(iv) Momentum conservation law in the liquid phase

$$(1 - \alpha_0 + \beta_1 \alpha_0) \frac{\partial u_{L1}}{\partial t_0} - \beta_1 \alpha_0 \frac{\partial u_{G1}}{\partial t_0} + (1 - \alpha_0) \frac{\partial p_{L1}}{\partial x_0} = 0, \tag{38}$$

(v) Modified Rayleigh–Plesset equation

$$R_1 + \frac{\Omega^2}{\Delta^2} p_{L1} = 0. \tag{39}$$

The set of linearized equations, i.e., Eqs. (35)–(39) contains five dependent variables (i.e., α_1 , p_{L1} , u_{G1} , u_{L1} and R_1). By eliminating α_1 , p_{L1} , u_{G1} and u_{L1} , the linear wave equation for the first-order perturbation of the bubble radius R_1 is derived as

$$\frac{\partial^2 R_1}{\partial t_0^2} - v_p^2 \frac{\partial^2 R_1}{\partial x_0^2} = 0, \tag{40}$$

where the phase velocity v_p is given by

$$v_p = \sqrt{\frac{3\alpha_0(1 - \alpha_0 + \beta_1)\gamma p_{G0} + \beta_1(1 - \alpha_0)\Delta^2/\Omega^2}{3\beta_1\alpha_0(1 - \alpha_0)}}. \tag{41}$$

Equation (40) indicates a linear and nondispersive wave motion, described in terms of t_0 and x_0 , while

Eq. (41) shows a proportional relation between the phase velocity v_p and $1/\sqrt{\alpha_0(1 - \alpha_0)}$, a feature similar to the classical speed of sound in bubbly liquids [14, 15]. The expressions in Eqs. (35)–(41) are identical to some of our previous results for the uncoated-bubble case [86, 87] but are different from other results [78, 93–95] that incorporate effects such as those of polydispersity, thermal effect, and drag force as well as results based on other shell models (the Church–Hoff and Chabouh models). This similarity indicates that if the same set of nondimensionalized parameters, i.e., Δ and Ω is used, the derived solution of the first-order problem will be identical to that of the uncoated bubble. However, because the expression of ω_B^* changes with the contribution of σ_0^* and χ^* , the behavior of the solution is different. By substituting the definitions of p_{G0} in Eq. (22), Δ in Eq. (33), and Ω in Eq. (34) into Eq. (41), we formulated a typical propagation speed U^* as follows:

$$U^* = \sqrt{\frac{3\alpha_0(1 - \alpha_0 + \beta_1)\gamma p_{G0}^*/\rho_{L0}^* + \beta_1(1 - \alpha_0)R_0^{*2}\omega_B^{*2}}{3\beta_1\alpha_0(1 - \alpha_0)v_p^2}}. \tag{42}$$

Focusing on the right-running wave in the leading-order of approximation, a phase function φ_0 for an arbitrary value of v_p can be introduced as follows:

$$\varphi_0 \equiv x_0 - v_p t_0. \tag{43}$$

By setting $R_1 \equiv f(\varphi_0; t_1, x_1)$, Eq. (40) becomes

$$\frac{\partial f}{\partial t_0} + v_p \frac{\partial f}{\partial x_0} = 0. \tag{44}$$

Rewriting Eqs. (35)–(39) using φ_0 and integrating them with respect to φ_0 , the other first-order perturbations α_1 , u_{G1} , u_{L1} and p_{L1} can be expressed in terms of $f(\varphi_0)$:

$$\begin{aligned} \alpha_1 &= s_1 f, & u_{G1} &= s_2 f, & u_{L1} &= s_3 f, & p_{L1} &= s_4 f, \\ s_4 &= -\frac{\Delta^2}{\Omega^2}, & s_1 &= \frac{(1 - \alpha_0)[3\beta_1\alpha_0 v_p^2 - (1 - \alpha_0)s_4]}{\alpha_0 v_p^2 (1 - \alpha_0 + \beta_1)}, \\ s_2 &= (s_1 - 3)v_p, & s_3 &= -\frac{\alpha_0 v_p}{1 - \alpha_0} s_1. \end{aligned} \tag{45}$$

Here, the integration constants are omitted because of the boundary conditions at $x_0 \rightarrow \infty$ where the bubbly liquid is uniform and at rest. Furthermore, from the relations in Eq. (45), it is apparent that the first-order perturbations in the near field characterized by t_0 and x_0 (i.e., α_1 , u_{G1} , u_{L1} , p_{L1} and R_1) are governed by Eq. (44).

3.2 Second order of approximation

Following the procedure presented in Sect. 3.1, but for the ϵ^2 terms, we derive a single inhomogeneous equation for R_2 :

$$\begin{aligned} \frac{\partial^2 R_2}{\partial t_0^2} - v_p^2 \frac{\partial^2 R_2}{\partial x_0^2} &= \frac{1}{3} \frac{\partial K_1}{\partial \varphi_0} - \frac{1}{3\alpha_0} \frac{\partial K_2}{\partial \varphi_0} \\ &+ \frac{1 - \alpha_0 + \beta_1}{3\beta_1(1 - \alpha_0)} \frac{\partial K_3}{\partial \varphi_0} + \frac{1}{3\alpha_0(1 - \alpha_0)} \frac{\partial K_4}{\partial \varphi_0} \\ &- \frac{1}{3\alpha_0} \frac{\Delta^2}{\Omega^2} \frac{\partial^2 K_5}{\partial \varphi_0^2} \equiv K(R_1; \varphi_0, t_1, x_1). \end{aligned} \tag{46}$$

The explicit form of inhomogeneous terms K_i ($i = 1, 2, 3, 4, 5$) is provided in ‘‘Appendix B’’. From the solvability condition of the inhomogeneous equation in Eq. (46), which is also the non-secular condition for the asymptotic expansions in Eqs. (16)–(21), we have $K = 0$, that is,

$$\begin{aligned} 2 \frac{\partial}{\partial \varphi_0} \left(\frac{\partial f}{\partial t_1} + \frac{\partial f}{\partial x_1} + \Pi_0 \frac{\partial f}{\partial \varphi_0} - \Pi_1 f \frac{\partial f}{\partial \varphi_0} \right. \\ \left. - \Pi_2 \frac{\partial^2 f}{\partial \varphi_0^2} + \Pi_3 \frac{\partial^3 f}{\partial \varphi_0^3} \right) = 0. \end{aligned} \tag{47}$$

Finally, through variable transformation,

$$\tau \equiv \epsilon t, \quad \xi \equiv x - (v_p + \epsilon \Pi_0)t, \tag{48}$$

the KdVB equation for nonlinear propagation in the far-field can be obtained as follows:

$$\frac{\partial f}{\partial \tau} - \Pi_1 f \frac{\partial f}{\partial \xi} - \Pi_2 \frac{\partial^2 f}{\partial \xi^2} + \Pi_3 \frac{\partial^3 f}{\partial \xi^3} = 0. \tag{49}$$

Here, Π_0, Π_1, Π_2 and Π_3 represent the advection, nonlinear, attenuation, and dispersion effects, respectively. The explicit forms of the coefficients Π_i ($i = 0, 1, 2, 3$) can be expressed as

$$\Pi_0 = - \frac{V^2}{6\alpha_0} \frac{\Delta^2}{\Omega^2} (1 - \alpha_0), \tag{50}$$

$$\begin{aligned} \Pi_1 = - \frac{1}{6} \left[k_1 - \frac{k_2}{\alpha_0} + \frac{(1 - \alpha_0 + \beta_1)k_3}{\beta_1(1 - \alpha_0)} + \frac{k_4}{\alpha_0(1 - \alpha_0)} \right. \\ \left. - \frac{\Delta^2}{\Omega^2} \frac{2k_5}{\alpha_0} \right], \end{aligned} \tag{51}$$

$$\Pi_2 = \frac{1}{6\alpha_0} (4\mu + 4\kappa_s), \tag{52}$$

$$\Pi_3 = \frac{\Delta^2}{6\alpha_0}, \tag{53}$$

where the explicit forms of k_i ($i = 1, 2, 3, 4, 5$) can be written as:

$$k_1 = 6(2 - s_1) + 2s_2(3 - s_1),$$

$$k_2 = -2\alpha_0 s_1 s_3,$$

$$\begin{aligned} k_5 = \frac{\Omega^2}{\Delta^2} \left[\frac{3\gamma(3\gamma + 1)p_{G0}}{2} \right. \\ \left. - \left(\frac{\Delta^2}{\Omega^2} - 3\gamma p_{G0} \right) \frac{N_{21} - N_1^2 + 1}{N_1 - 1} \right], \end{aligned}$$

$$\hat{k} = (\beta_1 + \beta_2)(s_2 - s_3)s_1 - \beta_1(s_2^2 - s_3^2),$$

$$k_3 = \hat{k} + 3\gamma p_{G0}(s_1 - 3\gamma - 1),$$

$$k_4 = -\alpha_0 \hat{k} + \alpha_0 s_1 s_4 - 2(1 - \alpha_0)s_3^2 - 2\alpha_0 s_1 s_3.$$

From this result, it is apparent that Π_0 is negative while Π_2 and Π_3 are positive. However, the sign of Π_1 is challenging to analyze; this case is evaluated with some examples in Sect. 4. A comparison with our previous results for the uncoated bubbles reveals certain discrepancies in the expressions of k_5 of Π_1 and Π_2 . The difference in k_5 of Π_1 originates from the complicated Marmottant–Gompertz surface tension model. Moreover, the difference in Π_2 arises from the incorporation of the shell dilatational viscosity κ_s^* , which leads to the additional nondimensional term κ_s , and the use of the modified Rayleigh–Plesset equation in Eq. (7) results in the omission of term $-\Delta^3 V / (6\alpha_0 \Omega^2)$. Notably, if we had followed the procedure presented in our previous paper using the Keller–Miksis equation to describe the bubble oscillation instead of the modified Rayleigh–Plesset equation, this term would have reappeared. Although the expressions for Π_0 and Π_3 are identical to those in our previous studies, these two coefficients implicitly depend on the presence of the shell through the change in the eigenfrequency ω_B^* .

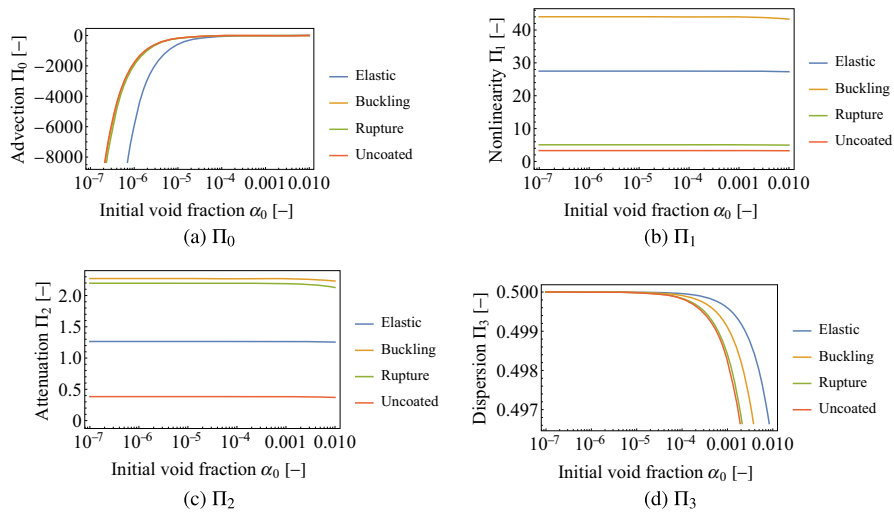


Fig. 3 Coefficients of the KdVB equation versus initial void fraction $\Pi_i(\alpha_0)$ curves for four different cases: elastic region ($\sigma_0^* = 0.036$: blue), buckled region ($\sigma_0^* = 0.001$: yellow), ruptured region ($\sigma_0^* = 0.071$: green) and uncoated case (red) for

$R_0^* = 1.5 \mu\text{m}$, $\kappa_s^* = 7.5 \times 10^{-9} \text{ kg/s}$, $\gamma = 1.07$, $c_{L0}^* = 1.5 \times 10^3 \text{ m/s}$, $p_{L0}^* = 101325 \text{ Pa}$, $\mu^* = 0.001 \text{ Pa} \cdot \text{s}$, $\rho_{L0}^* = 1000 \text{ kg/m}^3$, $\beta_1 = \beta_2 = 1/2$, $\epsilon = 0.0225$ and $\Omega = 1$. The high void fractions are graphed to demonstrate the behavior of the solutions

4 Discussion

4.1 Effect of shell

In this section, the effect of the initial surface tension on the coefficients of the derived KdVB equation is first investigated. For all the numerical calculations presented below, we set $v_p = 1$ because our method cannot predict the typical speed of sound in a bubbly liquid U^* . Figure 3 shows the coefficients versus the initial void fraction for the uncoated bubbles case (red) and three cases for lipid-shell encapsulated bubbles (i.e., near the buckled state, in elastic state, and near the ruptured state). The parameters used for each case are listed in Table 1. It should be noted that, in our calculation, the elasticity coefficient appears in denominators in certain relations and therefore zero value will make the program yields error. Here, since we would like to use the same model for every case (even for uncoated case) to avoid any unnecessary differences, the shell elasticity for uncoated bubble case is nonzero. Even though uncoated bubble case has shell elasticity, the contribution is negligible and the result for uncoated bubble case is the same with our previous studies [86]. In this range of parameters, the sign of Π_1 is positive for all the cases. Furthermore, Π_0 diverges rapidly as gas fraction goes to zero. This behavior arises from the divergence of typical wave velocity U^* chosen for

Table 1 Parameters used in the following discussion of the effect of initial surface tension

Case	$\sigma_0^* \text{ [N/m]}$	$\chi^* \text{ [N/m]}$	$\omega_B^* \text{ [rad/s]}$
Buckled	0.001	0.5	1.57×10^7
Elastic	0.036	0.5	2.81×10^7
Ruptured	0.071	0.5	1.62×10^7
Uncoated	0.072	0.0001	1.55×10^7

$v_p = 1$. For all terms except attenuation term Π_2 , the difference between the ruptured case (green) and the uncoated case (red) is relatively small. Moreover, the shell enhances all the effects of wave propagation, and for a larger void fraction, the absolute values of the coefficients decrease, although at different rates. It should be noted that, in medical applications and experimental studies, the void fraction is of the order of 10^{-6} . Although a higher void fraction is difficult to achieve in experiments and applications, we draw graphs at very high void fractions to illustrate the behavior of the solutions.

To investigate the effect of the initial surface tension σ_0^* on wave propagation, graphs of σ_0^* versus Π_i for different initial void fractions α_0 are plotted as solid lines in Fig. 4. The dashed line in Fig. 4 depicts the result of the coefficients Π_i subtracted by its counterpart in the uncoated bubbles case (at $\alpha_0 = 0.05$). Since for

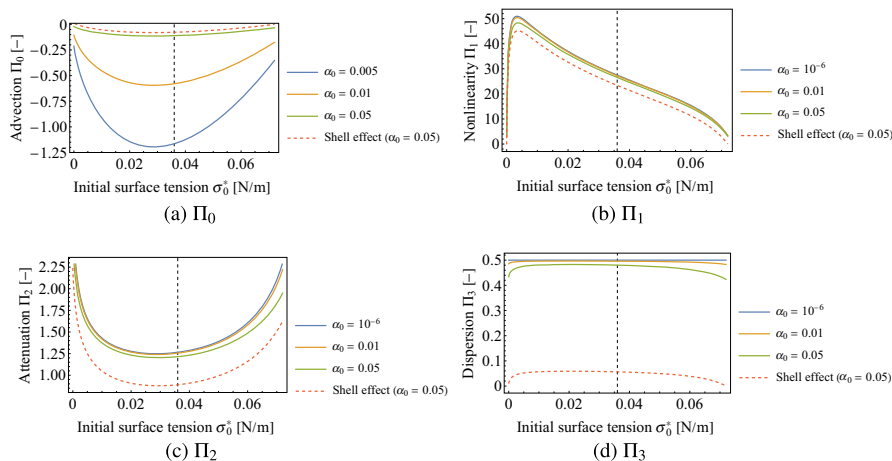


Fig. 4 Coefficients of the KdVB coefficient versus initial surface tension $\Pi_i(\sigma_0^*)$ curves of three different void fraction: $\alpha_0 = 10^{-6}$ (blue), $\alpha_0 = 0.01$ (orange) and $\alpha_0 = 0.05$ (green). The effects of the shell at $\alpha_0 = 0.05$ are indicated in the form of a red dashed

all σ_0^* , the coefficients of the KdVB equation for the uncoated bubble case do not vary, the dashed line in Fig. 4 is the $\alpha_0 = 0.05$ solid curve that shifts vertically and demonstrates the effect of the shell. From Fig. 4, we can deduce that the effect of the shell is relatively insignificant for the advection effect Π_0 near buckled and ruptured state, and dispersion effect Π_3 . However, for the attenuation effect Π_2 , the effect of the shell near buckled and ruptured state is significant. Moreover, for the nonlinear effect Π_1 , the effect of the shell is the main component. Another observation is that for the attenuation term Π_2 and dispersion term Π_3 , the coefficients vary insignificantly in the linear regime. In the linear-buckled and linear-ruptured transition regimes, $\sigma_0^* N_1$ and $\sigma_0^* N_{21}$ (i.e., the first- and second-order derivatives of the surface tension at $R^*/R_0^* = 1$) change rapidly, which may explain this tendency. From the expression of the coefficients, it is apparent that only N_1 affects the values of Π_0 , Π_2 , Π_3 through the change in ω_B^* , as discussed in Sect. 3. Therefore, these values were determined by N_1 . The coefficient N_{21} , however, implicitly defines the shape of the graphs because $\sigma_0^* N_{21}$ shows the rate of change of $\sigma_0^* N_1$. Physically, $\sigma_0^* N_1$ shows shell stiffness. For regions with high $\sigma_0^* N_1$, the shells are expected to be stiffer, making bubbles oscillation more difficult and impeding the rate of radius change of the bubbles. This tendency is reflected through the attenuation term Π_2 . As shown in Fig. 4c, the region of low absolute value of Π_2 corresponds to the region

line Shell effect is defined as Π_i subtracted by its counterpart in the uncoated bubbles case. The other parameters are same with Fig. 3. The high void fractions are graphed to show the behavior of the solutions

where shell stiffness is large. It should be noted that in our study, only the attenuation effect of shell viscosity and liquid near the bubbles are considered while other attenuation mechanisms such as thermal or radiation damping are neglected.

The behavior of the nonlinear term Π_1 is more complicated and is characterized by the absence of symmetry as in the other coefficients. Note that in the transition regime between linear-ruptured, an insignificant uphill region can be observed. These two features arise from the fact that the values of Π_0 , Π_2 and Π_3 are determined by N_1 and from the symmetry of N_1 , the graphs of these coefficients are symmetrical. However, the expression of component k_5 of Π_1 indicates that there is also a contribution of N_{21} . In the transition regime from the buckled state to the elastic state, $\sigma_0^* N_1$ changes rapidly from zero to χ^* (i.e., $\sigma_0^* N_{21}$ is positive), whereas in the transition regime from the elastic state to the ruptured state, $\sigma_0^* N_1$ changes rapidly back to zero (i.e., $\sigma_0^* N_{21}$ is negative). These rapid rates of change result in the dominance of $\sigma_0^* N_{21}$ in the nonlinear coefficient. For reference, we draw the ratio of $(\sigma_0^* N_{21})/(\sigma_0^* N_1)$ and present the result in Fig. 5.

4.2 Effect of upper and lower limits

To investigate the effect of the upper and lower limits of surface tension, each of the limit is removed by modifying the original Marmottant–Gompertz model. First,

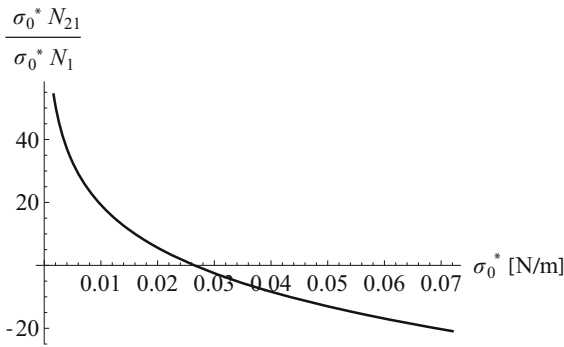


Fig. 5 Ratio of second-order derivative $\sigma_0^* N_{21}$ and first-order derivative $\sigma_0^* N_1$ of the initial surface tension at $R^*/R_0^* = 1$ for bubble radius $R_0^* = 1.5 \mu\text{m}$ and shell elasticity, $\chi^* = 0.5 \text{ N/m}$

Table 2 Parameters used in the study of removing the upper and lower limits of surface tension

Case	A [N/m]	$\sigma_c^{* \prime}$ [N/m]	$\sigma_0^{* \prime}$ [N/m]	$\chi^{* \prime}$ [N/m]
Remove upper limit	–	800	σ_0^*	400
Remove lower limit	800	$\sigma_c^* + A$	$\sigma_0^* + A$	3000

the upper limit is removed by setting asymptote value (i.e., free gas–water surface tension σ_c^*) to a higher value while maintaining the lower limit. Second, the lower limit is removed while maintaining the upper limit through two steps: (i) The graph is translated down A unit (i.e., $\sigma^{* \prime} = -A + \sigma^*$); (ii) The values of the surface tension (i.e., σ_c^* and σ_0^*) are set to a new value according to A (i.e., $\sigma_c^{* \prime}$ to $\sigma_c^{* \prime} = \sigma_c^* + A$ and $\sigma_0^{* \prime}$ to $\sigma_0^{* \prime} = \sigma_0^* + A$). It should be noted that the change in the values of surface tension only occurs in the expansion terms of surface tension σ^* and therefore, does not affect the zero-order term. In addition, the value of χ^* is varied to obtain a good fit to the elastic region of the original model. The new parameters are listed in Table 2.

The modified models, after the removal of the limits, are shown in Fig. 6. Notably, since the Marmottant–Gompertz model is based on the Gompertz function, it uses three parameters: an asymptote parameter, a displacement along the horizontal-axis parameter, and a growth rate parameter. The Marmottant–Gompertz model varies these three parameters through $(\sigma_0^*, \sigma_c^*$ and $\chi^*)$, and only two parameters can be set since we have already fixed σ_0^* . This results in high values of $\chi^{* \prime}$ used in this section. Moreover, we cannot find a set of parameters that can remove both the upper and lower limits with which the linear region is comparable with

the original model. Therefore, a direct comparison for the case of the surface model without upper and lower limits cannot be achieved in this study, and readers are referred to our previous papers [77–79] for the results of the analysis using the Church–Hoff shell model.

In Figs. 7 and 8, the results for the upper-limit-removed case and original case are illustrated as dashed curves and solid curves, respectively. In Fig. 7, there is a shift in the ruptured case toward a higher absolute value for Π_0, Π_1 , and Π_3 , whereas for the attenuation term Π_2 , the ruptured case moves toward a smaller absolute value. The relatively small differences in Π_0, Π_2 , and Π_3 for elastic lines and buckled lines between two cases may arise from the small discrepancies between the upper-limit-removed model and the original model, specifically the value of $\sigma_0^* N_1$ (i.e., the slope of the graph). However, the considerable difference in the nonlinear coefficient Π_1 might be the result of two factors: the difference in $\sigma_0^* N_1$ and the difference in $\sigma_0^* N_{21}$. Because the value and variation of $\sigma_0^* N_1$ are insignificant, the difference in $\sigma_0^* N_{21}$ for each case is dominant in determining the difference in Π_1 , as mentioned in Sect. 4.1. In Fig. 8, the case of $\alpha_0 = 10^{-6}, 0.01$ is omitted to highlight the results. The significant shape change for all coefficients can be explained as follows. Since the differences in $\sigma_0^* N_1$ and the differences in $\sigma_0^* N_{21}$ between the elastic and ruptured regimes are small for upper-limit-removed case, the curves of coefficients flatten in the region with a relatively large value of σ_0^* . This illustrates our discussion of the effects of $\sigma_0^* N_1$ and $\sigma_0^* N_{21}$ on the wave propagation coefficients.

In Figs. 9 and 10, the results for the lower-limit-removed case and original case are illustrated as dashed curves and solid curves, respectively. In Fig. 9, the buckling curves vary significantly while the elastic and rupture curves do not vary significantly for Π_0, Π_2 and Π_3 . This is expected owing to the dependence of those curves on the slope of σ^* . By removing the lower limit, the slope of σ^* ($\sigma_0^* N_1$) near the buckled region becomes larger than the original case, explaining the lower dissipation absolute value for the buckling curve, since a stiffer shell makes bubbles harder to compress. The notable differences of the Π_1 curves can be explained similarly with the upper-limit-removed case. In Fig. 10, the $\Pi_i(\sigma_0^*)$ curves are plotted. A similar trend with the upper-limit-removed case can be observed. However, in this case the curves flatten in the region with a relatively large σ_0^* value.

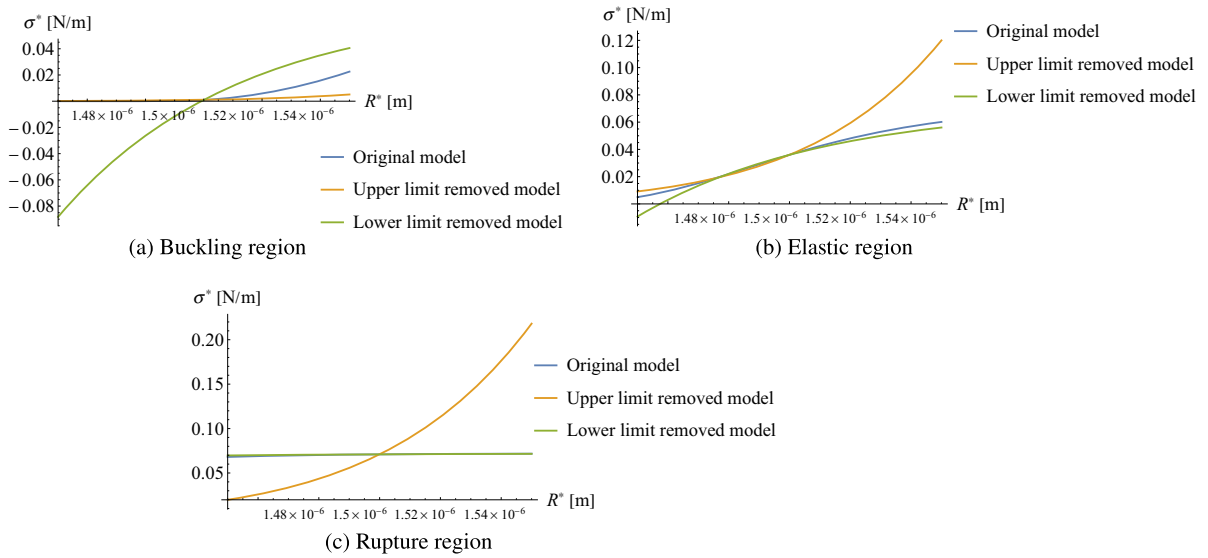


Fig. 6 Comparison of surface tension models in different regimes. The original Marmottant–Gompertz model, upper limit removed model, lower limit removed model as blue, orange, and green curves, respectively

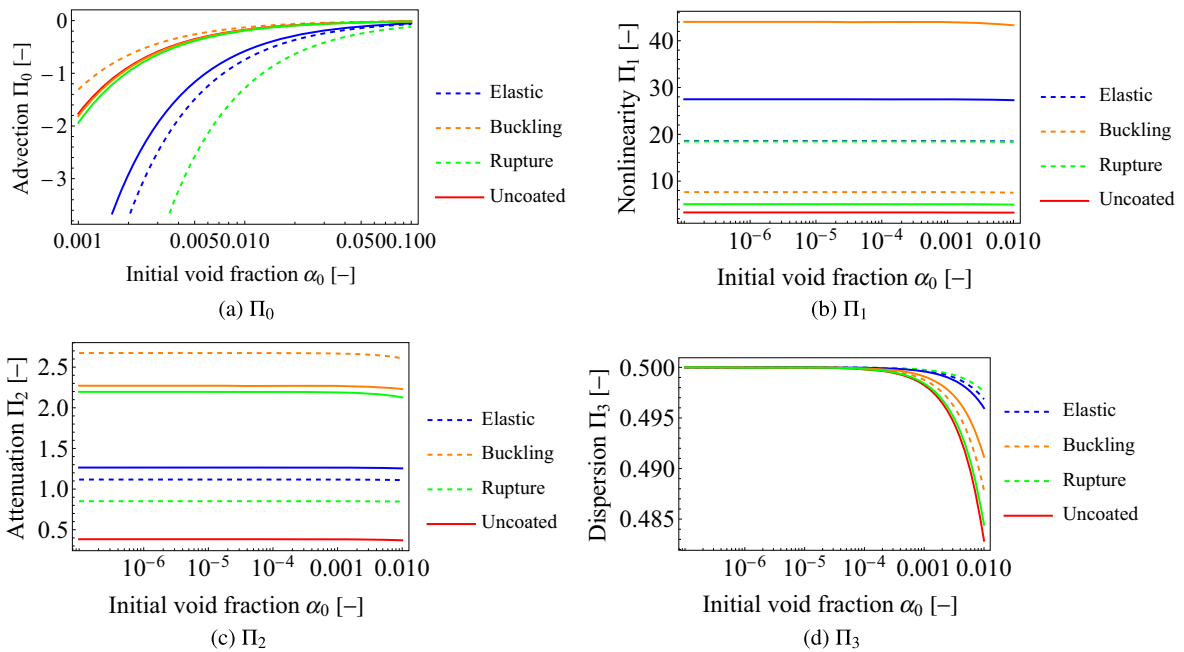


Fig. 7 Coefficients of the KdVB equation versus initial void fraction $\Pi_i(\alpha_0)$ curves for four different cases: elastic region ($\sigma_0^* = 0.036$: blue), buckled region ($\sigma_0^* = 0.001$: yellow), ruptured region ($\sigma_0^* = 0.071$: green) and uncoated case (red). The

dashed curves represent the case where upper limit was removed, and the solid curves represent the original model. The other parameters are same with Fig. 3. The high void fractions are graphed to demonstrate the behavior of the solutions

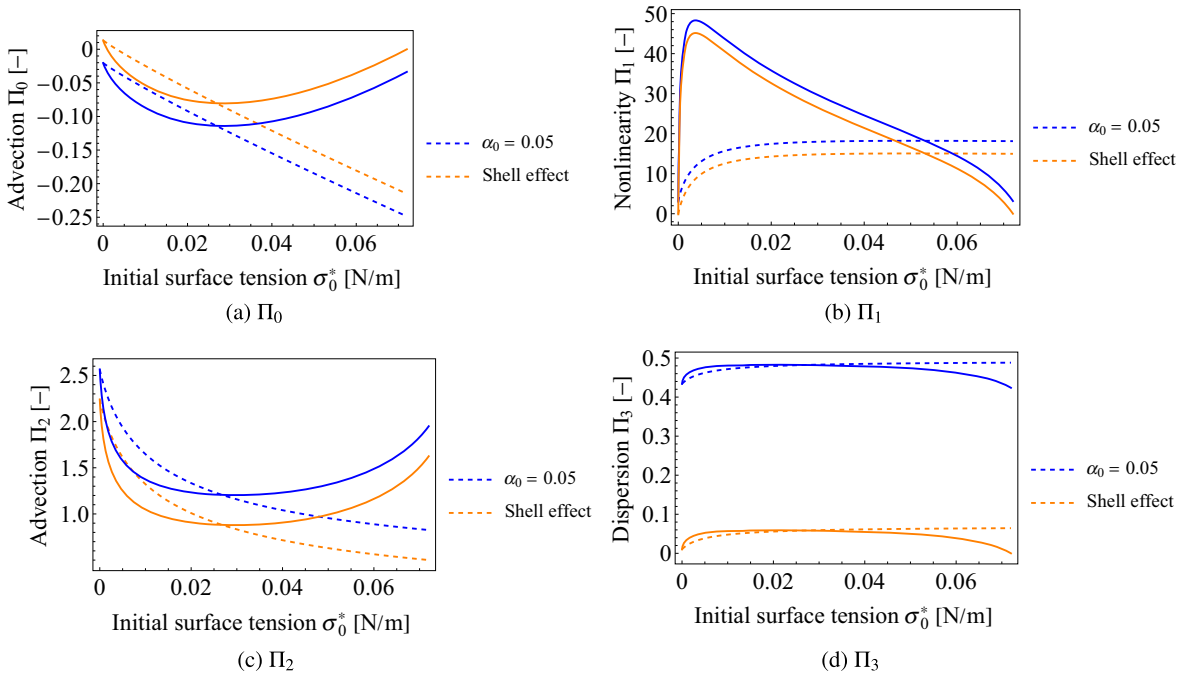


Fig. 8 Coefficients of the KdVB equation versus initial surface tension $\Pi_i(\sigma_0^*)$ curves of $\alpha_0 = 0.05$ (blue) and the effects of the shell at $\alpha_0 = 0.05$ (orange). The curves denoted as “Shell effect” represent difference of Π_i ’s value for coated bubble case and that for uncoated bubble case. The dashed curves and solid

curves represent the case where upper limit was removed, and the original model, respectively. The other parameters are same with Fig. 3. The high void fractions are graphed to demonstrate the behavior of the solutions

4.3 Limitations of the present model

The KdVB equation in Eq. (49) incorporates the Marmottant–Gompertz model proposed by Gümmer et al. [85], and a same set of parameters was used to define and calculate the surface tension curve. Figure 5 shows that in Marmottant–Gompertz model, $\sigma_0^* N_{21}$ is an order of magnitude larger than $\sigma_0^* N_1$. However, Sijl et al. [48] demonstrated that $\sigma_0^* N_{21}$ must be at least

encapsulated microbubbles [48] and corresponds with the experimentally determined value. From our analysis, it is noted that a change in $\sigma_0^* N_{21}$ directly changes the value of the nonlinear coefficient Π_1 and affects the tendency of $\Pi_i(\sigma_0^*)$ graphs. The alternative model, which can control the slope of surface tension curve and its rate of change, was proposed by Sijl et al. [48]. They introduced a new parameter (i.e., ζ to manipulate $\sigma_0^* N_{21}$), and the model is shown as follows:

$$\sigma^*(R) = \begin{cases} 0 & (R^* < R_{\text{buck}}^*), \\ \zeta^*/2 (R^*/R_{\text{buck}}^* - 1)^2 & (R_{\text{buck}}^* < R^* < R_{\text{elas}}^*), \\ 2\chi_{\text{max}}^* (R^*/R_0^* - 1) & (R_{\text{elas}}^* < R^* < R_{\text{elas}2}^*), \\ \sigma_c^* - \zeta^*/2 (R^*/R_{\text{buck}}^* - R_{\text{rupt}}^*/R_{\text{buck}}^*)^2 & (R_{\text{elas}2}^* < R^* < R_{\text{rupt}}^*), \\ \sigma_c^* & (R^* > R_{\text{rupt}}^*), \end{cases} \quad (54)$$

three orders of magnitude larger than $\sigma_0^* N_1$ to illustrate the abrupt elasticity change of the collapsing phospholipid monolayer. This characteristic is crucial for explaining the subharmonic behavior of phospholipid-

In this study, we did not use the model proposed by Sijl et al. [48] since it requires the analysis to be conducted for each separated region; this is because, in this model, the surface tension is divided into different

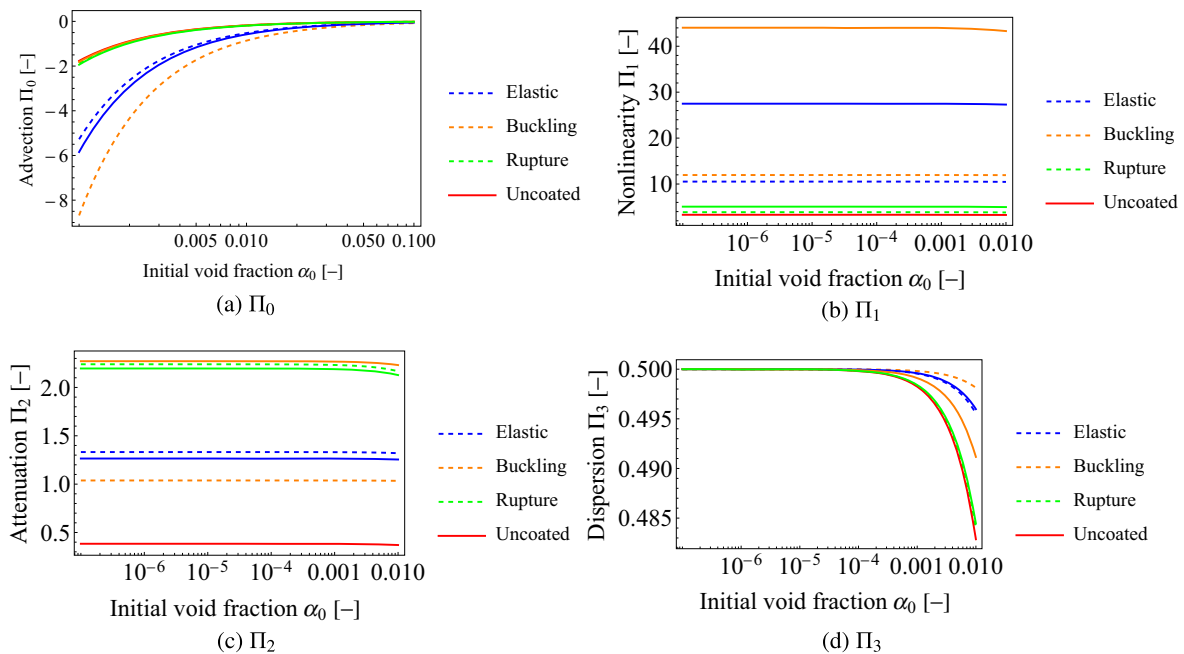


Fig. 9 Coefficients of the KdVB equation versus initial void fraction $\Pi_i(\alpha_0)$ curves for four different cases: elastic region ($\sigma_0^* = 0.036$: blue), buckled region ($\sigma_0^* = 0.001$: yellow), ruptured region ($\sigma_0^* = 0.071$: green) and uncoated case (red).

The dashed curves represent the case where the lower limit was removed, and the solid curves represent the original model. The other parameters are same with Fig. 3. The high void fractions are graphed to demonstrate the behavior of the solutions

regions, which are expressed using different equations. Furthermore, in each separated region, there may not be sufficient information about the other regions. For example, in the region of $R_{\text{elas}2}^*$, there is no information about the upper limit (i.e., σ_c^*).

Additionally, the KdVB equation derived in this study neglects the contributions of several factors. For instance, the effect of the bubble–bubble interaction, [96–98] that changes the resonance frequency of the bubbles, can alter the coefficients of the KdVB equation. Such interactions have been shown to affect the oscillation of the microbubbles, resulting in milder pulsation, and reduction in minimum pressure threshold at resonance [99, 100]. Furthermore, Sojahrood et al. [76, 101] proved theoretically and experimentally that the bubble–bubble interaction is crucial even at low concentrations and influences the pressure-dependent attenuation and sound speed of the bubbly liquid significantly. This effect explains the increase in scattering power until a plateau with increasing void fraction and then decrease, as predicted in [55] and observed experimentally in [102]. Therefore, the bubble–bubble inter-

action will be addressed in future studies, particularly for the void fraction curves.

Certain assumptions mentioned in Sect. 2, such as the initial uniform bubble radius distribution, thermal effect, and drag force acting on the bubbles for uncoated bubbles, have been considered in our previous studies [94, 103, 104]. Since the inclusion of the aforementioned effects may obscure the effects of buckling and rupture, these effects are excluded from this study.

5 Conclusions and prospect for future research

Using multiple-scale analysis for the weakly nonlinear propagation of one-dimensional ultrasound, we derived a KdVB equation. This equation characterizes wave propagation based on advection, nonlinear, attenuation, and dispersion effects. The analysis showed that shell with buckling and rupture phenomena increases the absolute values of all the effects through the increase in eigenfrequency caused by the elastic coefficient and variation of surface tension value. Moreover, the behavior of the nonlinear term is significantly affected by the

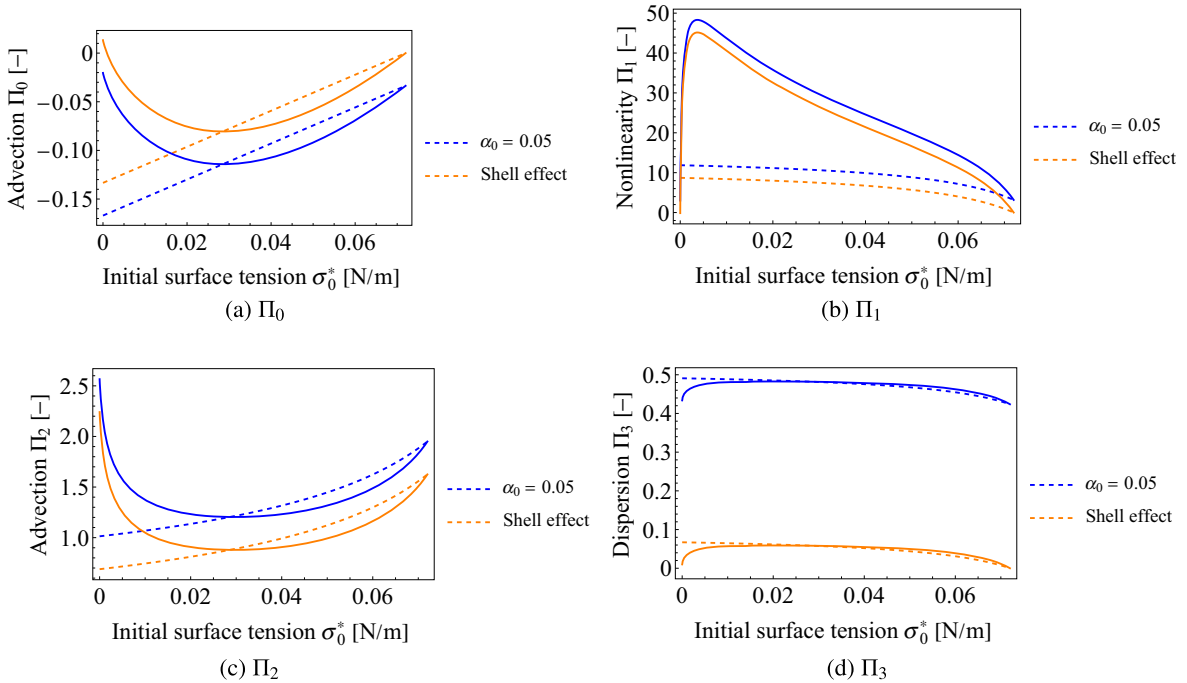


Fig. 10 Coefficients of the KdVB equation versus initial surface tension $\Pi_i(\sigma_0^*)$ curves of $\alpha_0 = 0.05$ (blue) and the effects of the shell at $\alpha_0 = 0.05$ (orange). The curves denoted as “Shell effect” represent difference of Π_i ’s value for coated bubble case and that for uncoated bubble case. The dashed curves and solid

curves represent the case where the lower limit was removed and original model case, respectively. The other parameters are same with Fig. 3. The high void fractions are graphed to demonstrate the behavior of the solutions

rate of change of the elastic coefficient. For the dispersion terms, the shell contribution is relatively small, whereas for the attenuation, the contribution is medium, more prominent near buckled and ruptured states, and for nonlinear term the contribution of the shell is dominant.

From these results, a basic understanding of the effect of the phospholipid shell on the nonlinear propagation of ultrasound was obtained. In the future, analysis of ultrasound propagation incorporating other shell models and other assumptions, such as bubble–bubble interaction and effect of non-Newtonian fluid [52], will be conducted. Numerical simulations, evaluation of the stability of solutions, and inclusion of elastic continuum mechanics, such as plastic deformation and anisotropy [41], will also be considered. Finally, a comprehensive model including the investigated assumptions will be proposed.

Acknowledgements We would like to thank referees for their valuable comments and suggestions, and Editage (www.editage.com) for English language editing.

Author contributions All author contributed equally.

Funding This work was partially carried out with the aid of the JSPS KAKENHI (22K03898), based on results obtained from a project subsidized by the New Energy and Industrial Technology Development Organization (NEDO)(JPNP20004), and Ono Charitable Trust for Acoustics and supported by JKA and its promotion funds from KEIRIN RACE.

Data availability The data that support the findings of this study are available from the corresponding author upon reasonable request.

Declarations

Competing interests The authors declare that they have no known competing financial interests or personal relationships that could have appeared to influence the work reported in this paper.

Open Access This article is licensed under a Creative Commons Attribution 4.0 International License, which permits

use, sharing, adaptation, distribution and reproduction in any medium or format, as long as you give appropriate credit to the original author(s) and the source, provide a link to the Creative Commons licence, and indicate if changes were made. The images or other third party material in this article are included in the article's Creative Commons licence, unless indicated otherwise in a credit line to the material. If material is not included in the article's Creative Commons licence and your intended use is not permitted by statutory regulation or exceeds the permitted use, you will need to obtain permission directly from the copyright holder. To view a copy of this licence, visit <http://creativecommons.org/licenses/by/4.0/>.

Appendices

A Marmottant–Gompertz model

The full form of Marmottant–Gompertz model [85] is given as follows:

$$\sigma^* = \sigma_c^* \exp \left\{ \ln \left(\frac{\sigma_0^*}{\sigma_c^*} \right) \exp \left[\frac{2e\chi^*}{\sigma_c^*} \sqrt{1 + \frac{\sigma_c^*}{2\chi^*} \left(\frac{R_0^*}{R_{\text{buck}}^*} - \frac{R^*}{R_{\text{buck}}^*} \right)} \right] \right\}, \quad (\text{A.1})$$

where σ_0^* is the initial surface tension at $R^* = R_0^*$, σ_c^* is the surface tension of the clean gas–liquid interface, χ^* is the surface elasticity of the lipid monolayer, and R_{buck}^* can be expressed as:

$$R_{\text{buck}}^* = \frac{R_0^*}{\sqrt{1 + \sigma_0^*/\chi^*}}. \quad (\text{A.2})$$

Although not shown in Eq. (A.1), it is helpful to show the radius at which the bubble begins to rupture, that is, rupture radius:

$$R_{\text{rupt}}^* = R_{\text{buck}}^* \sqrt{1 + \frac{\sigma_c^*}{\chi^*}} = R_0^* \sqrt{\frac{1 + \sigma_c^*/\chi^*}{1 + \sigma_0^*/\chi^*}}. \quad (\text{A.3})$$

By using equation for balance of the normal stress in Eq. (11) and modified Rayleigh–Plesset equation in Eq. (7), we have the following equation:

$$\begin{aligned} \rho_{L0}^* R^* \frac{D_G^2 R^*}{Dt^{*2}} + \rho_{L0}^* \frac{3}{2} \left(\frac{D_G R^*}{Dt^*} \right)^2 &= p_G^* - p_L^* \\ - \frac{2\sigma^*(R^*)}{R^*} - \frac{4\mu^* D_G R^*}{R^* Dt^*} - \frac{4k_s^* D_G R^*}{R^{*2} Dt^*} & \\ + \frac{R^* D_G}{c_{L0}^* Dt^*} p_G^* &. \end{aligned} \quad (\text{A.4})$$

Finally, we can express the surface tension term in Eq. (A.4) by Eq. (A.1) and we obtain the full form of the equation for spherical oscillations of bubbles.

B Inhomogeneous terms

The inhomogeneous terms K_i ($i = 1, 2, 3, 4, 5$) in Eq. (46) are given by

$$K_1 = -\frac{\partial u_{G1}}{\partial x_1} + \frac{\partial}{\partial t_1} (3R_1 - \alpha_1) + 3 \frac{\partial R_1 (\alpha_1 - 2R_1)}{\partial t_0} + \frac{\partial}{\partial x_0} [u_{G1} (3R_1 - \alpha_1)], \quad (\text{B.1})$$

$$K_2 = (1 - \alpha_0) \frac{\partial u_{L1}}{\partial x_1} - \alpha_0 \frac{\alpha_1}{\partial t_1} - \alpha_0 \frac{\partial \alpha_1 u_{L1}}{\partial x_0} + (1 - \alpha_0) \frac{\partial p_{L1}}{\partial t_0}, \quad (\text{B.2})$$

$$\begin{aligned} K_3 &= 3\gamma p_{G0} \frac{\partial R_1}{\partial x_1} - \beta_1 \frac{\partial}{\partial t_1} (u_{G1} - u_{L1}) \\ &\quad - \beta_1 \left(u_{G1} \frac{\partial u_{G1}}{\partial x_0} - u_{L1} \frac{\partial u_{L1}}{\partial x_0} \right) \\ &\quad - \beta_1 \alpha_1 \frac{\partial}{\partial t_0} (u_{G1} - u_{L1}) - \beta_2 (u_{G1} - u_{L1}) \frac{\partial \alpha_1}{\partial t_0} \\ &\quad + 3\gamma p_{G0} \left[\alpha_1 \frac{\partial R_1}{\partial x_0} - (3\gamma + 1) R_1 \frac{\partial R_1}{\partial x_0} \right], \end{aligned} \quad (\text{B.3})$$

$$\begin{aligned} K_4 &= -(1 - \alpha_0) \left(\frac{\partial p_{L1}}{\partial x_1} + \frac{\partial u_{L1}}{\partial t_1} \right) \\ &\quad + \beta_1 \alpha_0 \frac{\partial}{\partial t_1} (u_{G1} - u_{L1}) + \alpha_0 \frac{\partial \alpha_1 u_{L1}}{\partial t_0} \\ &\quad + \beta_1 \alpha_0 \left(u_{G1} \frac{\partial u_{G1}}{\partial x_0} - u_{L1} \frac{\partial u_{L1}}{\partial x_0} \right) \\ &\quad + \beta_1 \alpha_0 \alpha_1 \frac{\partial}{\partial t_0} (u_{G1} - u_{L1}) + \beta_2 \alpha_0 (u_{G1} - u_{L1}) \frac{\partial \alpha_1}{\partial t_0} \\ &\quad + \alpha_0 \alpha_1 \frac{\partial p_{L1}}{\partial x_0} - (1 - \alpha_0) \frac{\partial u_{L1}^2}{\partial x_0} \\ &\quad + \alpha_0 \left(p_{L1} + \frac{\Delta^2}{\Omega^2} R_1 \right) \frac{\partial \alpha_1}{\partial x_0}, \end{aligned} \quad (\text{B.4})$$

$$\begin{aligned} K_5 &= \frac{9\gamma^2 + 3\gamma - 2(\Delta^2/\Omega^2 - 3\gamma p_{G0})(N_{21} - N_1^2 + 1)/(N_1 - 1)}{2\Delta^2/\Omega^2} R_1^2 \\ &\quad - \Omega^2 \frac{\partial^2 R_1}{\partial t_0^2} - 4(\mu + \kappa_s) \frac{\Omega^2}{\Delta^2} \frac{\partial R_1}{\partial t_0}. \end{aligned} \quad (\text{B.5})$$

References

1. Rayleigh, L., VIII.: On the pressure developed in a liquid during the collapse of a spherical cavity. The London, Edinburgh, And Dublin Philosophical Magazine And Journal Of Science. **34**, 94–98 (1917)
2. Plesset, M.: The Dynamics of Cavitation Bubbles. American Society of Mechanical Engineers (1949)
3. Trilling, L.: The collapse and rebound of a gas bubble. J. Appl. Phys. **23**, 14–17 (1952)
4. Keller, J., Kolodner, I.: Damping of underwater explosion bubble oscillations. J. Appl. Phys. **27**, 1152–1161 (1956)
5. Eller, A.: Damping constants of pulsating bubbles. J. Acoust. Soc. Am. **47**, 1469–1470 (1970)

6. Prosperetti, A.: Nonlinear oscillations of gas bubbles in liquids: steady-state solutions. *J. Acoust. Soc. Am.* **56**, 878–885 (1974)
7. Prosperetti, A.: Nonlinear oscillations of gas bubbles in liquids. Transient solutions and the connection between subharmonic signal and cavitation. *J. Acoust. Soc. Am.* **57**, 810–821 (1975)
8. Lauterborn, W.: Numerical investigation of nonlinear oscillations of gas bubbles in liquids. *J. Acoust. Soc. Am.* **59**, 283–293 (1976)
9. Keller, J., Miksis, M.: Bubble oscillations of large amplitude. *J. Acoust. Soc. Am.* **68**, 628–633 (1980)
10. Prosperetti, A., Lezzi, A.: Bubble dynamics in a compressible liquid. Part 1. First-order theory. *J. Fluid Mech.* **168**, 457–478 (1986)
11. Prosperetti, A.: The equation of bubble dynamics in a compressible liquid. *Phys. Fluids* **30**, 3626–3628 (1987)
12. Van Wijngaarden, L.: On the collective collapse of a large number of gas bubbles in water. *Appl. Mech.*, pp. 854–861 (1966)
13. Van Wijngaarden, L.: Linear and non-linear dispersion of pressure pulses in liquid bubble mixtures. In: 6th Symposium on Naval Hydrodynamics, pp. 115–128 (1966)
14. Van Wijngaarden, L.: On the equations of motion for mixtures of liquid and gas bubbles. *J. Fluid Mech.* **33**, 465–474 (1968)
15. Van Wijngaarden, L.: One-dimensional flow of liquids containing small gas bubbles. *Annu. Rev. Fluid Mech.* **4**, 369–396 (1972)
16. Caffisch, R., Miksis, M., Papanicolaou, G., Ting, L.: Wave propagation in bubbly liquids at finite volume fraction. *J. Fluid Mech.* **160**, 1–14 (1985)
17. Caffisch, R.: Global existence for a nonlinear theory of bubbly liquids. *Commun. Pure Appl. Math.* **38**, 157–166 (1985)
18. Caffisch, R., Miksis, M., Papanicolaou, G., Ting, L.: Effective equations for wave propagation in bubbly liquids. *J. Fluid Mech.* **153**, 259–273 (1985)
19. Christiansen, C., Kryvi, H., Sontum, P., Skotland, T.: Physical and biochemical characterization of Albunex, a new ultrasound contrast agent consisting of air-filled albumin microspheres suspended in a solution of human albumin. *Biotechnol. Appl. Biochem.* **19**, 307–320 (1994)
20. Cohen, J., Cheirif, J., Segar, D., Gillam, L., Gottdiener, J., Hausnerova, E., Bruns, D.: Improved left ventricular endocardial border delineation and opacification with Optison (FS069), a new echocardiographic contrast agent: results of a phase III multicenter trial. *J. Am. Coll. Cardiol.* **32**, 746–752 (1998)
21. Kaul, S.: Myocardial contrast echocardiography: a 25-year retrospective. *Circulation* **118**, 291–308 (2008)
22. Lindner, J.: ‘Principles of contrast echocardiography. Essential echocardiography: a companion To Braunwald’s heart disease, pp. 27–33 (2019)
23. Lindner, J., Kaul, S.: Delivery of drugs with ultrasound. *Echocardiography* **18**, 329–337 (2001)
24. Tachibana, K., Tachibana, S.: The use of ultrasound for drug delivery. *Echocardiography* **18**, 323–328 (2001)
25. Frenkel, V.: Ultrasound mediated delivery of drugs and genes to solid tumors. *Adv. Drug Deliv. Rev.* **60**, 1193–1208 (2008)
26. Martins, A., Ahmed, S., Vitor, R., Hussein, G.: *Ultrasonic Drug Delivery Using Micelles and Liposomes*. Springer, Berlin (2016)
27. Nakata, M., Tanimura, N., Koyama, D., Krafft, M.: Adsorption and desorption of a phospholipid from single microbubbles under pulsed ultrasound irradiation for ultrasound-triggered drug delivery. *Langmuir* **35**, 10007–10013 (2019)
28. Van Wamel, A., Kooiman, K., Hartevelde, M., Emmer, M., Folkert, J., Versluis, M., De Jong, N.: Vibrating microbubbles poking individual cells: drug transfer into cells via sonoporation. *J. Control. Release* **112**, 149–155 (2006)
29. Karshafian, R., Bevan, P., Williams, R., Samac, S., Burns, P.: Sonoporation by ultrasound-activated microbubble contrast agents: effect of acoustic exposure parameters on cell membrane permeability and cell viability. *Ultrasound Med. Biol.* **35**, 847–860 (2009)
30. Peruzzi, G., Sinibaldi, G., Silvani, G., Ruocco, G., Casciola, C.: Perspectives on cavitation enhanced endothelial layer permeability. *Colloids Surf. B Biointerfaces* **168**, 83–93 (2018)
31. Jong, N., Hoff, L., Skotland, T., Bom, N.: Absorption and scatter of encapsulated gas filled microspheres: theoretical considerations and some measurements. *Ultrasonics* **30**, 95–103 (1992)
32. De Jong, N., Hoff, L.: Ultrasound scattering of Albunex® microspheres. *Ultrasonics*, pp. 175–181 (1993)
33. De Jong, N., Cornet, R., Lancée, C.: Higher harmonics of vibrating gas-filled microspheres. Part one: simulations. *Ultrasonics* **32**, 447–453 (1994)
34. De Jong, N., Cornet, R., Lancee, C.: Higher harmonics of vibrating gas-filled microspheres. Part two: measurements. *Ultrasonics* **32**, 455–459 (1994)
35. Church, C.: The effects of an elastic solid surface layer on the radial pulsations of gas bubbles. *J. Acoust. Soc. Am.* **97**, 1510–1521 (1995)
36. Roy, R., Church, C., Calabrese, A.: *Cavitation Produced by Short Pulses of Ultrasound*. Elsevier, Amsterdam (1990)
37. Hoff, L., Sontum, P., Hovem, J.: Oscillations of polymeric microbubbles: effect of the encapsulating shell. *J. Acoust. Soc. Am.* **107**, 2272–2280 (2000)
38. Sarkar, K., Shi, W., Chatterjee, D., Forsberg, F.: Characterization of ultrasound contrast microbubbles using in vitro experiments and viscous and viscoelastic interface models for encapsulation. *J. Acoust. Soc. Am.* **118**, 539–550 (2005)
39. Marmottant, P., Van Der Meer, S., Emmer, M., Versluis, M., De Jong, N., Hilgenfeldt, S., Lohse, D.: A model for large amplitude oscillations of coated bubbles accounting for buckling and rupture. *J. Acoust. Soc. Am.* **118**, 3499–3505 (2005)
40. Doinikov, A., Haac, J., Dayton, P.: Modeling of nonlinear viscous stress in encapsulating shells of lipid-coated contrast agent microbubbles. *Ultrasonics* **49**, 269–275 (2009)
41. Chabouh, G., Dollet, B., Quilliet, C., Coupier, G.: Spherical oscillations of encapsulated microbubbles: effect of shell compressibility and anisotropy. *J. Acoust. Soc. Am.* **149**, 1240–1257 (2021)

42. Doinikov, A., Bouakaz, A.: Review of shell models for contrast agent microbubbles. *IEEE Trans. Ultrason. Ferroelectr. Freq. Control* **58**, 981–993 (2011)
43. Faez, T., Emmer, M., Kooiman, K., Versluis, M., Steen, A., Jong, N.: 20 years of ultrasound contrast agent modeling. *IEEE Trans. Ultrason. Ferroelectr. Freq. Control* **60**, 7–20 (2012)
44. Dollet, B., Marmottant, P., Garbin, V.: Bubble dynamics in soft and biological matter. *Annu. Rev. Fluid Mech.* **51**, 331–355 (2019)
45. Versluis, M., Stride, E., Lajoinie, G., Dollet, B., Segers, T.: Ultrasound contrast agent modeling: a review. *Ultrasound Med. Biol.* **46**, 2117–2144 (2020)
46. Chatterjee, A., Chatterjee, D.: Analytical investigation of hydrodynamic cavitation control by ultrasonics. *Nonlinear Dyn.* **46**, 179–194 (2006)
47. Overvelde, M., Garbin, V., Sijl, J., Dollet, B., De Jong, N., Lohse, D., Versluis, M.: Nonlinear shell behavior of phospholipid-coated microbubbles. *Ultrasound Med. Biol.* **36**, 2080–2092 (2010)
48. Sijl, J., Dollet, B., Overvelde, M., Garbin, V., Rozendal, T., De Jong, N., Lohse, D., Versluis, M.: Subharmonic behavior of phospholipid-coated ultrasound contrast agent microbubbles. *J. Acoust. Soc. Am.* **128**, 3239–3252 (2010)
49. Frinking, P., Gaud, E., Brochot, J., Arditi, M.: Subharmonic scattering of phospholipid-shell microbubbles at low acoustic pressure amplitudes. *IEEE Trans. Ultrason. Ferroelectr. Freq. Control* **57**, 1762–1771 (2010)
50. Katiyar, A., Sarkar, K.: Excitation threshold for subharmonic generation from contrast microbubbles. *J. Acoust. Soc. Am.* **130**, 3137–3147 (2011)
51. Katiyar, A., Sarkar, K.: Effects of encapsulation damping on the excitation threshold for subharmonic generation from contrast microbubbles. *J. Acoust. Soc. Am.* **132**, 3576–3585 (2012)
52. Behnia, S., Mobadersani, F., Yahyavi, M., Rezavand, A.: Chaotic behavior of gas bubble in non-Newtonian fluid: a numerical study. *Nonlinear Dyn.* **74**, 559–570 (2013)
53. Sojahrood, A., Falou, O., Earl, R., Karshafian, R., Kolios, M.: Influence of the pressure-dependent resonance frequency on the bifurcation structure and backscattered pressure of ultrasound contrast agents: a numerical investigation. *Nonlinear Dyn.* **80**, 889–904 (2015)
54. Hegedűs, F., Kalmár, C.: Dynamic stabilization of an asymmetric nonlinear bubble oscillator. *Nonlinear Dyn.* **94**, 307–324 (2018)
55. Sojahrood, A., Earl, R., Haghi, H., Li, Q., Porter, T., Kolios, M., Karshafian, R.: Nonlinear dynamics of acoustic bubbles excited by their pressure-dependent subharmonic resonance frequency: influence of the pressure amplitude, frequency, encapsulation and multiple bubble interactions on oversaturation and enhancement of the subharmonic signal. *Nonlinear Dyn.* **103**, 429–466 (2021)
56. Sojahrood, A., Haghi, H., Karshafian, R., Kolios, M.: Nonlinear dynamics and bifurcation structure of ultrasonically excited lipid coated microbubbles. *Ultrason. Sonochem.* **72**, 105405 (2021)
57. Doinikov, A., Novell, A., Escoffre, J., Bouakaz, A.: Encapsulated bubble dynamics in imaging and therapy. *Bubble Dyn. Shock Waves*, 259–289 (2013)
58. Borden, M.: Intermolecular forces model for lipid microbubble shells. *Langmuir* **35**, 10042–10051 (2018)
59. Chabouh, G., Elburg, B., Versluis, M., Segers, T., Quilliet, C., Coupier, G.: Buckling of lipidic ultrasound contrast agents under quasi-static load. *Philos. Trans. Royal Soc. A* **381**, 2244 (2023)
60. Orsi, M., Haubertin, D., Sanderson, W., Essex, J.: A quantitative coarse-grain model for lipid bilayers. *J. Phys. Chem. B* **112**, 802–815 (2008)
61. Duncan, S., Larson, R.: Folding of lipid monolayers containing lung surfactant proteins SP-B1-25 and SP-C studied via coarse-grained molecular dynamics simulations. *Biochimica Et Biophysica Acta (BBA)-Biomembranes* **1798**, 1632–1650 (2010)
62. Orsi, M., Michel, J., Essex, J.: Coarse-grain modelling of DMPC and DOPC lipid bilayers. *J. Phys. Condens. Matter* **22**, 155106 (2010)
63. Orsi, M., Essex, J.: The ELBA force field for coarse-grain modeling of lipid membranes. *PLoS ONE* **6**, e28637 (2011)
64. Qin, S., Caskey, C., Ferrara, K.: Ultrasound contrast microbubbles in imaging and therapy: physical principles and engineering. *Phys. Med. Biol.* **54**, R27 (2009)
65. Renaud, G., Bosch, J., Ten Kate, G., Shamdasani, V., Entekin, R., Jong, N., Steen, A.: Counter-propagating wave interaction for contrast-enhanced ultrasound imaging. *Phys. Med. Biol.* **57**, L9 (2012)
66. Maresca, D., Skachkov, I., Renaud, G., Jansen, K., Soest, G., Jong, N., Steen, A.: Imaging microvasculature with contrast-enhanced ultraharmonic ultrasound. *Ultrasound Med. Biol.* **40**, 1318–1328 (2014)
67. Zhu, J., Tagawa, N.: High resolution ultrasonic imaging based on frequency sweep in both of transducer element domain and imaging line domain. *Jpn. J. Appl. Phys.* **58**, SGGE03 (2019)
68. Ma, J., Yu, J., Fan, Z., Zhu, Z., Gong, X., Du, G.: Acoustic nonlinearity of liquid containing encapsulated microbubbles. *J. Acoust. Soc. Am.* **116**, 186–193 (2004)
69. Xia, L.: Theoretical estimation of attenuation coefficient of resonant ultrasound contrast agents. *J. Acoust. Soc. Am.* **147**, 3061–3071 (2020)
70. Louisnard, O.: A simple model of ultrasound propagation in a cavitating liquid. Part I: theory, nonlinear attenuation and traveling wave generation. *Ultrason. Sonochem.* **19**, 56–65 (2012)
71. Louisnard, O., Garcia-Vargas, I.: Simulation of sonoactors accounting for dissipated power. *Energy Asp. Acoust. Cavit. Sonochem.*, 219–249 (2022)
72. Jamshidi, R., Brenner, G.: Dissipation of ultrasonic wave propagation in bubbly liquids considering the effect of compressibility to the first order of acoustical Mach number. *Ultrasonics* **53**, 842–848 (2013)
73. Sojahrood, A., Haghi, H., Karshafian, R., Kolios, M.: Critical corrections to models of nonlinear power dissipation of ultrasonically excited bubbles. *Ultrason. Sonochem.* **66**, 105089 (2020)
74. Sojahrood, A., Haghi, H., Karshafian, R., Kolios, M.: Nonlinear model of acoustical attenuation and speed of sound in a bubbly medium. In: 2015 IEEE International Ultrasonics Symposium (IUS), pp. 1–4 (2015)
75. Sojahrood, A., Haghi, H., Li, Q., Porter, T., Karshafian, R., Kolios, M.: Nonlinear power loss in the oscillations

- of coated and uncoated bubbles: role of thermal, radiation and encapsulating shell damping at various excitation pressures. *Ultrason. Sonochem.* **66**, 105070 (2020)
76. Sojahrood, A., Li, Q., Haghi, H., Karshafian, R., Porter, T., Kolios, M.: Probing the pressure dependence of sound speed and attenuation in bubbly media: experimental observations, a theoretical model and numerical calculations. *Ultrason. Sonochem.* **95**, 106319 (2023)
 77. Kikuchi, Y., Kanagawa, T.: Weakly nonlinear theory on ultrasound propagation in liquids containing many microbubbles encapsulated by visco-elastic shell. *Jpn. J. Appl. Phys.* **60**, SDDD14 (2021)
 78. Kikuchi, Y., Kanagawa, T., Ayukai, T.: Physico-mathematical model for multiple ultrasound-contrast-agent microbubbles encapsulated by a visco-elastic shell: effect of shell compressibility on ultrasound attenuation. *Chem. Eng. Sci.* **269**, 117541 (2023)
 79. Kanagawa, T., Honda, M., Kikuchi, Y.: Nonlinear acoustic theory on flowing liquid containing multiple microbubbles coated by a compressible visco-elastic shell: Low and high frequency cases. *Phys. Fluids* **35**, 023303 (2023)
 80. De Jong, N., Emmer, M., Chin, C., Bouakaz, A., Mastik, F., Lohse, D., Versluis, M.: Compression-only behavior of phospholipid-coated contrast bubbles. *Ultrasound Med. Biol.* **33**, 653–656 (2007)
 81. Emmer, M., Vos, H., Goertz, D., Wamel, A., Versluis, M., Jong, N.: Pressure-dependent attenuation and scattering of phospholipid-coated microbubbles at low acoustic pressures. *Ultrasound Med. Biol.* **35**, 102–111 (2009)
 82. Meer, S., Dollet, B., Voormolen, M., Chin, C., Bouakaz, A., Jong, N., Versluis, M., Lohse, D.: Microbubble spectroscopy of ultrasound contrast agents. *J. Acoust. Soc. Am.* **121**, 648–656 (2007)
 83. Emmer, M., Van Wamel, A., Goertz, D., De Jong, N.: The onset of microbubble vibration. *Ultrasound Med. Biol.* **33**, 941–949 (2007)
 84. Sojahrood, A., Haghi, H., Porter, T., Karshafian, R., Kolios, M.: Experimental and numerical evidence of intensified non-linearity at the microscale: the lipid coated acoustic bubble. *Phys. Fluids* **33**, 072006 (2021)
 85. Gümmer, J., Schenke, S., Denner, F.: Modelling lipid-coated microbubbles in focused ultrasound applications at subresonance frequencies. *Ultrasound Med. Biol.* **47**, 2958–2979 (2021)
 86. Kanagawa, T., Yano, T., Watanabe, M., Fujikawa, S.: Unified theory based on parameter scaling for derivation of nonlinear wave equations in bubbly liquids. *J. Fluid Sci. Technol.* **5**, 351–369 (2010)
 87. Yano, T., Kanagawa, T., Watanabe, M., Fujikawa, S.: Nonlinear wave propagation in bubbly liquids. *Bubble Dyn. Shock Waves*, 107–140 (2013)
 88. Egashira, R., Yano, T., Fujikawa, S.: Linear wave propagation of fast and slow modes in mixtures of liquid and gas bubbles. *Fluid Dyn. Res.* **34**, 317–334 (2004)
 89. Yano, T., Egashira, R., Fujikawa, S.: Linear analysis of dispersive waves in bubbly flows based on averaged equations. *J. Phys. Soc. Jpn.* **75**, 104401 (2006)
 90. Zhang, D., Prosperetti, A.: Averaged equations for inviscid disperse two-phase flow. *J. Fluid Mech.* **267**, 185–219 (1994)
 91. Eames, I., Hunt, J.: Forces on bodies moving unsteadily in rapidly compressed flows. *J. Fluid Mech.* **505**, 349–364 (2004)
 92. Jeffrey, A., Kawahara, T.: *Asymptotic Methods in Nonlinear Wave Theory*. *Applicable Mathematics Series* (1982)
 93. Yatabe, T., Kanagawa, T., Ayukai, T.: Theoretical elucidation of effect of drag force and translation of bubble on weakly nonlinear pressure waves in bubbly flows. *Phys. Fluids* **33**, 033315 (2021)
 94. Arai, S., Kanagawa, T., Ayukai, T.: Nonlinear pressure waves in bubbly flows with drag force: theoretical and numerical comparison of acoustic and thermal and drag force dissipations. *J. Phys. Soc. Jpn.* **91**, 043401 (2022)
 95. Kanagawa, T., Ishitsuka, R., Arai, S., Ayukai, T.: Contribution of initial bubble radius distribution to weakly nonlinear waves with a long wavelength in bubbly liquids. *Phys. Fluids* **34**, 103320 (2022)
 96. Heckman, C., Rand, R.: Dynamics of microbubble oscillators with delay coupling. *Nonlinear Dyn.* **71**, 121–132 (2013)
 97. Fuster, D., Conoir, J., Colonius, T.: Effect of direct bubble-bubble interactions on linear-wave propagation in bubbly liquids. *Phys. Rev. E* **90**, 063010 (2014)
 98. Garashchuk, I., Kazakov, A., Sinelshchikov, D.: Synchronous oscillations and symmetry breaking in a model of two interacting ultrasound contrast agents. *Nonlinear Dyn.* **101**, 1199–1213 (2020)
 99. Guédra, M., Cornu, C., Insera, C.: A derivation of the stable cavitation threshold accounting for bubble-bubble interactions. *Ultrason. Sonochem.* **38**, 168–173 (2017)
 100. Yasui, K., Lee, J., Tuziuti, T., Towata, A., Kozuka, T., Iida, Y.: Influence of the bubble–bubble interaction on destruction of encapsulated microbubbles under ultrasound. *J. Acoust. Soc. Am.* **126**, 973–982 (2009)
 101. Sojahrood, A., Li, Q., Haghi, H., Karshafian, R., Porter, T., Kolios, M.: Investigation of the nonlinear propagation of ultrasound through a bubbly medium including multiple scattering and bubble-bubble interaction: theory and experiment. In: 2017 IEEE International Ultrasonics Symposium (IUS), pp. 1–4 (2017)
 102. Martinez, P., Bottenus, N., Borden, M.: Cavitation characterization of size-isolated microbubbles in a vessel phantom using focused ultrasound. *Pharmaceutics* **14**, 1925 (2022)
 103. Kamei, T., Kanagawa, T., Ayukai, T.: An exhaustive theoretical analysis of thermal effect inside bubbles for weakly nonlinear pressure waves in bubbly liquids. *Phys. Fluids* **33**, 053302 (2021)
 104. Kagami, S., Kanagawa, T.: Weakly nonlinear propagation of focused ultrasound in bubbly liquids with a thermal effect: derivation of two cases of Khokolov–Zabolotskaya–Kuznetsov equations. *Ultrason. Sonochem.* **88**, 105911 (2022)

Publisher's Note Springer Nature remains neutral with regard to jurisdictional claims in published maps and institutional affiliations.